Multibody System Dynamics
https://doi.org/10.1007/s11044-024-09990-4

RESEARCH

Numerical simulation of the post-derailment behaviour of a railway vehicle and its interaction with the infrastructure

Matteo Santelia[1] · Francesco Mazzeo[1] · Riccardo Rosi[1] · Egidio Di Gialleonardo[1] · Stefano Melzi[1] · Stefano Bruni[1]

Received: 21 December 2023 / Accepted: 22 April 2024

Abstract
Train derailments may have catastrophic consequences, and therefore suitable measures should be designed and installed at specific safety-relevant sites to mitigate their effects. Mitigation measures, such as guard rails and containment walls, aim at restraining the motion of the derailed vehicle using suitable derailment containment devices. However, the design and structural sizing of these devices is challenging as the quantification of the loads caused by the impact with the vehicle is complex.

The aim of this paper is to extend previous work from the same authors aimed at defining a non-linear multi-body model for the simulation in time-domain of the post-derailment behaviour of a railway vehicle and the impact on a derailment containment wall. The extension presented in this paper is concerned with the model of the interaction of the derailed vehicle with the sleepers and with the ballast. To this aim, an algorithm is introduced to manage the different possible contact conditions the wheels of the vehicle may undergo during the derailment process: contact with the rail, with the sleepers and with the ballast. Then, a model of the impact between the derailed wheels and the sleepers is introduced, and a terramechanic model defining the forces acting on the wheels sinking in the ballast is established. The effect of the accurate modelling of forces exchanged by the derailed wheels with the sleepers and the ballast is quantified for a relevant derailment scenario and shown to be highly relevant to the estimation of the impact loads applied to the containment structure.

Keywords Train derailment · Post-derailment dynamics · Derailment containment structure · Multi-body · Sleeper-impact · Wheel–ballast contact · Terramechanics

1 Introduction

Train derailments may have catastrophic consequences for passengers' safety, and they also cause significant economic losses, infrastructure damage and service disruption. The increase in train service speed, especially in the high-speed sector, has led this problem to become more and more critical, especially in regard of passenger's safety. For this reason,

✉ M. Santelia
matteo.santelia@polimi.it

[1] Department of Mechanical Engineering, Politecnico di Milano, Via La Masa, 1 1 I-20156 Milan, Italy

Published online: 13 May 2024

the railway industry has increasingly focused on understanding the causes of derailments [1] and on finding measures to avoid them [2, 3]. In modern railways, advanced signalling and traffic control systems and improved design and maintenance methods for both the rolling stock and infrastructure have been introduced, leading to substantial improvement of safety. Yet, derailments still occasionally occur due to various reasons, which can be ascribed to human error, poor infrastructure condition, mechanical failures, impact with obstacles or even earthquakes [4–7].

The consequences of a derailment can be particularly dangerous and severe when this safety-critical event occurs at specific locations in a railway line, e.g. viaducts, stations and areas where the railway track is close to surrounding domestic or industrial buildings. At these sensitive locations, specific measures must be adopted to mitigate the outcome of a derailment. A solution presented in [8] is to install in the bogie frame a guidance designed to constrain the lateral motion of the vehicle after a derailment has occurred. Another possibility is to use parts of the running gear such as brake discs, gearboxes or bogie frames to obtain a similar guidance effect [9]. A final option is to adopt infrastructure-based devices: in this regard, both guard-rails and containment walls have been studied. In [10] guard-rails placed between running rails are studied to prevent secondary damage caused by derailed trains on high-risk lines, whereas in [11, 12] the containment capacity and crash-worthiness of a derailment containment wall (DCW) is evaluated using a finite element (FE) analysis to perform a collision simulation. Some experiments have been carried out to reproduce and analyse controlled derailments and different measures to mitigate them [1, 13]. However, it is extremely challenging and expensive to perform in-field tests of this type. Therefore, numerical simulations are mainly used to study derailment events and to design suitable mitigation measures [6, 8].

Regarding the interaction between a ballasted track and a derailed vehicle, a limited number of studies exist in literature. In [14] a simplified model that considers a relationship between friction coefficients and slip rates for a typical ballasted track is proposed, while in [15] the ballast layer is modelled using nonlinear continuous viscoelastic elements. In [6, 16] a similar approach is presented for a slab track, in which the vertical wheel-slab force is a function of the relative displacement between the wheel and the slab, while the tangential component of the contact force is defined according to Coulomb dry friction theory.

As far as wheels-sleeper interaction is concerned, references [8, 17] present a FE model to obtain pre-defined look-up tables of forces during wheel's impact. This model has been validated by comparing indentation marks from a real derailment event. However, in these works contact with the ballast is not considered.

The aim of this paper is to introduce a non-linear multi-body (MB) model for the simulation in time domain of the post-derailment behaviour of a railway vehicle and its interaction with the infrastructure, consisting of sleepers and ballast, and finally the impact with a DCW.

The work presented here builds on previous research presented in [18] where the equations of motion of the vehicle and the model of the impact with the DCW are developed, whilst this paper focuses on developing models for the interaction of the derailed wheels with the ballast and sleepers. An algorithm is introduced to manage the different conditions that each wheel may encounter during the derailment phase, which may consist of contact with the rail, with the sleepers or with the ballast. An impact model is introduced to represent the contact of a derailed wheel with the sleepers, and a terramechanic approach based on Bekker's semi-empirical model [19] for the normal pressures and on Janosi–Hanamoto's law [20] for the tangential stresses is proposed to simulate the interaction of the wheel with the ballast. A comparison is shown between numerical results from the model and experimental results from a derailment test performed on a test circuit. Finally, the model is applied to the study of a derailment scenario for a high-speed vehicle.

2 Model of the vehicle and of the impact with the derailment containment wall

The proposed train model considers a single vehicle with one carbody, two bogies and four wheelsets, all considered as rigid bodies. Each body has six degrees of freedom (DOF), resulting in a total of 42 DOF system. Each bogie is connected to two wheelsets by primary suspensions and to the carbody by secondary suspensions. The suspensions (both primary and secondary) are modelled by a set of massless visco-elastic elements with non-linear characteristics defined in the form of force-deformation or force-velocity curves. The equations of motion of the vehicle before the impact with the DCW are as follows:

$$\boldsymbol{M}(\boldsymbol{x})\,\ddot{\boldsymbol{x}} = \boldsymbol{Q}_{\boldsymbol{v}}(\boldsymbol{x},\dot{\boldsymbol{x}}) + \boldsymbol{Q}(\boldsymbol{x},\dot{\boldsymbol{x}},t)\,, \tag{1}$$

where $\boldsymbol{x}$ is the vector collecting the 42 independent coordinates of the system, $\boldsymbol{M}(\boldsymbol{x})$ is the configuration-dependent mass matrix of the vehicle, $\boldsymbol{Q}_{\boldsymbol{v}}$ is the quadratic velocity vector accounting for gyroscopic effects and $\boldsymbol{Q}$ is the vector of the generalised forces acting on the vehicle. This latter term can be in turn expressed as the sum of the contribution of different forces acting on the system:

$$\boldsymbol{Q}(\boldsymbol{x},\dot{\boldsymbol{x}},t) = \boldsymbol{Q}_{\boldsymbol{g}} + \boldsymbol{Q}_{\boldsymbol{s}}(\boldsymbol{x},\dot{\boldsymbol{x}}) + \boldsymbol{Q}_{\boldsymbol{c}}(\boldsymbol{x},\dot{\boldsymbol{x}},t) + \boldsymbol{Q}_{\boldsymbol{w-s}}(\boldsymbol{x},\dot{\boldsymbol{x}}) + \boldsymbol{Q}_{\boldsymbol{w-b}}(\boldsymbol{x},\dot{\boldsymbol{x}})\,, \tag{2}$$

where $\boldsymbol{Q}_{\boldsymbol{g}}$ is a constant vector defining the effect of weight on each body, $\boldsymbol{Q}_{\boldsymbol{s}}$ is the vector of generalised forces produced by suspension components, $\boldsymbol{Q}_{\boldsymbol{c}}$ is the vector of generalised forces arising from the wheel–rail contact, which is active only while each wheel is in contact with the corresponding rail. This vector explicitly depends on time due to the time-varying curvature and superelevation of the track. Finally, terms $\boldsymbol{Q}_{\boldsymbol{w-s}}$ and $\boldsymbol{Q}_{\boldsymbol{w-b}}$ are the generalised forces representing the interaction of the derailed wheels with the sleepers and the ballast respectively. Equation (1) is integrated numerically in the time domain using an Adams–Bashforth–Moulton algorithm [21, 22]. The simulation is implemented in MATLAB.

The expressions of the mass matrix $\boldsymbol{M}$ and of vectors $\boldsymbol{Q}_{\boldsymbol{v}}$ and $\boldsymbol{Q}_{\boldsymbol{g}}$ are derived according to standard multi-body techniques as described in [23]. Suspension components are modelled as non-linear compact force (CMP) elements [24], which allows to consider the stiffness or viscous damping properties along three directions defined in a component-specific reference system. Wheel–rail contact forces $\boldsymbol{Q}_{\boldsymbol{c}}$ are introduced according to a simplified model based on contact tables in order to obtain a good trade-off between a fast and accurate estimation. The detailed derivation of terms $\boldsymbol{Q}_{\boldsymbol{s}}$ and $\boldsymbol{Q}_{\boldsymbol{c}}$ is provided in [18], whilst the derivation of terms $\boldsymbol{Q}_{\boldsymbol{w-s}}$ and $\boldsymbol{Q}_{\boldsymbol{w-b}}$ is provided in Sect. 3 of this paper.

During the derailment phase, the motion of a set of candidate impact points in the vehicle is considered, and the onset of a contact with the DCW is checked for each candidate contact point at each time step of the numerical simulation. Once a contact with the DCW is detected, an additional vector of generalised forces $\boldsymbol{Q}_{\boldsymbol{i,v}}$ is introduced in the equations of motion of the vehicle to consider the Lagrangian components of the impact forces on the independent coordinates of the vehicle. At the same time, a new set of equations is added to equation (1) to represent the motion of the DCW impacted by the vehicle. The dynamic behaviour of the DCW is represented using a structural FE model based on the use of plate elements, more information about the FE model of the DCW is provided in Sect. 4. The system of equations describing the dynamics of the vehicle together with the impacted DCW

therefore becomes:

$$\begin{aligned} \boldsymbol{M}(\boldsymbol{x})\,\ddot{\boldsymbol{x}} &= \boldsymbol{Q}_v(\boldsymbol{x},\dot{\boldsymbol{x}}) + \boldsymbol{Q}(\boldsymbol{x},\dot{\boldsymbol{x}},t) + \boldsymbol{Q}_{i,v}(\boldsymbol{x},\dot{\boldsymbol{x}},\boldsymbol{x}_s,\dot{\boldsymbol{x}}_s) \\ \boldsymbol{M}_s\ddot{\boldsymbol{x}}_s &= -\boldsymbol{K}_s\boldsymbol{x}_s - \boldsymbol{R}_s\dot{\boldsymbol{x}}_s + \boldsymbol{Q}_{i,s}(\boldsymbol{x},\dot{\boldsymbol{x}},\boldsymbol{x}_s,\dot{\boldsymbol{x}}_s), \end{aligned} \tag{3}$$

where $\mathbf{x_s}$ is the vector of nodal coordinates of the DCW model, $\boldsymbol{M}_s$, $\boldsymbol{R}_s$ and $\boldsymbol{K}_s$ are respectively the mass, damping and stiffness matrices of the DCW, which are derived using standard FE techniques for Kirchoff plate elements [25] and $\boldsymbol{Q}_{i,s}$ is the vector of nodal forces representing the effect of the impact on the DCW. The derivation of this term and of vector $\boldsymbol{Q}_{i,v}$ is presented in [18].

Equations (3) are used to simulate the final phase of the derailment process, consisting of the impact with the DCW, and allow to estimate the impact force between the vehicle and the wall.

As a post-processing of these results, the time history of the bending moment at the base of the DCW can be obtained, which is used for the structural sizing of the wall. To this aim, the bending moment $M_{y,k}$ in each kth plate element located at the base of the DCW is obtained from the following equation [26, 27]:

$$M_{y,k} = -D\left(\frac{\partial^2 w(x,y)}{\partial y^2} + \nu\frac{\partial^2 w(x,y)}{\partial x^2}\right) = -D\left(\frac{\partial^2 \boldsymbol{\phi}_k^T}{\partial y^2} + \nu\frac{\partial^2 \boldsymbol{\phi}_k^T}{\partial x^2}\right)\boldsymbol{x}_{s,k}, \tag{4}$$

where D is the flexural rigidity of the elementary plate element, $\boldsymbol{\phi_k}$ is a vector of shape functions for the kth plate element in the model of the DCW [25] and $\boldsymbol{x}_{s,k}$ is the vector of nodal displacements for the same kth element. The flexural rigidity parameter D is defined as follows:

$$D = \frac{Et^3}{12(1-\nu^2)}, \tag{5}$$

where t is the thickness of the plate. The total bending moment at the base of the DCW is then obtained as

$$M_{tot} = \sum_k \int_0^{l_k} M_{y,k}(x)\,dx, \tag{6}$$

where l_k is the horizontal length of the kth finite element.

3 Model of the interaction between the track and the derailed vehicle: ballast and sleepers

This section presents the contact models considering the interaction of the derailed wheels with the sleepers and the ballast, corresponding to terms $\boldsymbol{Q}_{w-s}$ and $\boldsymbol{Q}_{w-b}$ in equation (2).

Two distinct models are introduced to consider:

1) Wheel–sleeper interaction;
2) Wheel–ballast interaction.

A contact management algorithm is used to consider the contact of each wheel with either the corresponding rail or with the sleepers and the ballast after derailment. This algorithm is called by the multi-body solver at each integration time-step and for each wheel. It consists

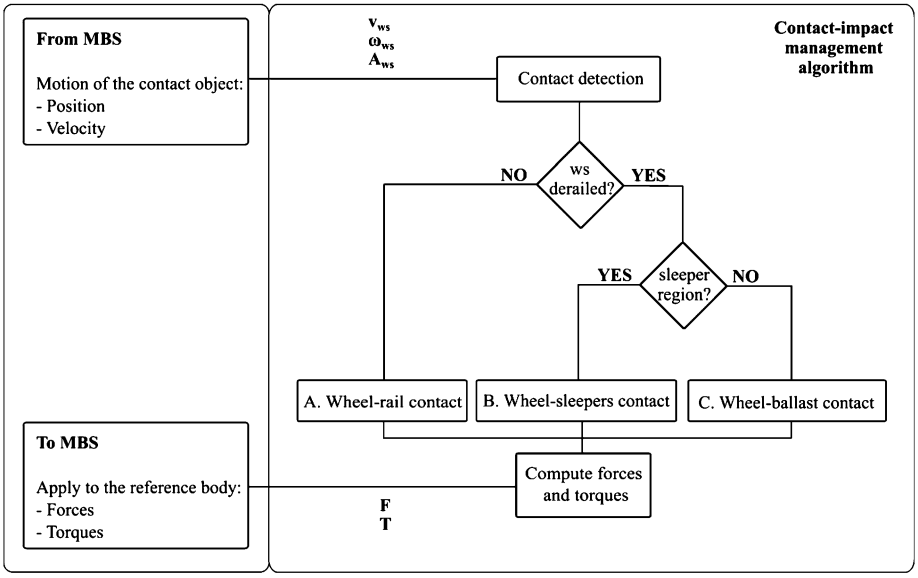

Fig. 1 Flowchart of the contact management algorithm

of the simple syntax tree shown in Fig. 1, using as an input the instantaneous position of the wheel centre and determining which one of the three contact conditions takes place for the wheel (see Fig. 2):

1) wheel in contact with the rail, no derailment has occurred so far, corresponding to the block labelled as (A) in the figure;
2) wheel in contact with a sleeper (after the derailment has occurred), corresponding to the block labelled as (B) in the figure;
3) wheel in contact with the ballast (after the derailment has occurred and the wheel has travelled a sufficiently large distance in the local lateral direction), corresponding to the block labelled as (C) in the figure.

The transition from one to another of the above cases is considered to take place instantaneously, reflecting the physical discontinuities among the three contact conditions.

The algorithm first checks if the lateral wheel/rail relative displacement exceeds a threshold value implemented in the contact table used to compute wheel/rail contact forces, see [18] for more details. If this threshold is not exceeded, the wheel is in contact with the corresponding rail, block (A) of the flowchart, and the forces acting on the wheel due to the contact with the rail are computed according to the standard wheel–rail algorithm presented in [18].

If the above threshold is exceeded, the lateral distance of the wheel centre from the track centreline is compared to the upper and lower thresholds corresponding to the lateral width of the sleeper. In case the lateral distance of the wheel centre falls within the range defined by these upper/lower thresholds, the wheel is in contact with the sleepers, block (B) of the flowchart, and the forces acting on the wheel are computed according to the model described in Sect. 3.1. In this condition the derailed wheel is assumed to be in contact only with the sleepers. This assumption is justified by the fact that the upper surface of the sleepers is elevated compared to the ballast by approximately 30 mm in the Italian high-speed (HS)

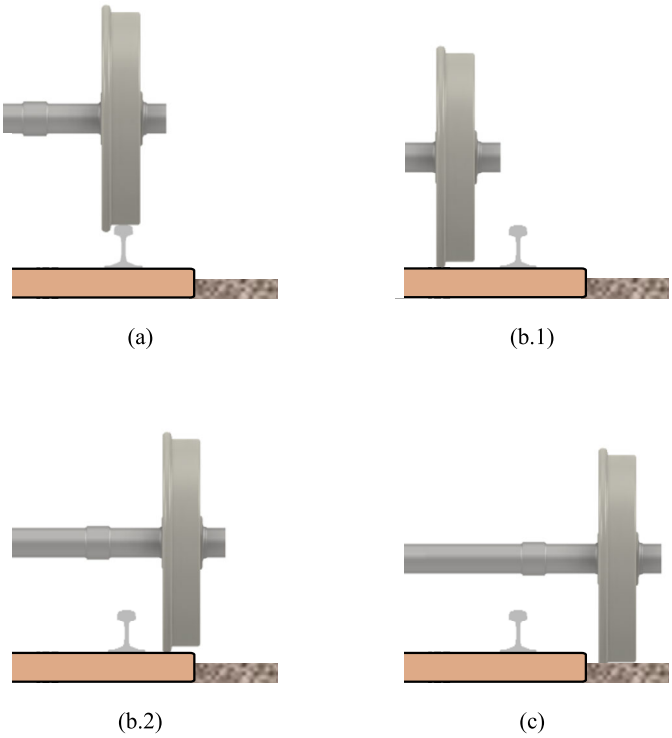

Fig. 2 Different possible contact conditions of the wheel: (a) wheel–rail contact, (b.1) wheel–sleeper contact, wheel between the rails (b.2) wheel–sleeper contact, wheel outside the rails and (c) wheel–ballast contact

lines, with the aim of mitigating the flying ballast issue. If otherwise the lateral distance of the wheel centre from the track falls outside the above-described range, the wheel is in contact with the ballast, block (C) of the flowchart, and the forces acting on the wheel are computed using the method presented in Sect. 3.2.

3.1 Wheel–sleeper interaction algorithm

The sleepers are modelled considering a periodic vertical profile rigidly fixed to the ground (see Fig. 3). The inclusion in the model of the effects related to the flexibility of the sleeper supports is envisaged as a possible future extension. At each time step of the integration, the vector of the vehicle coordinates $\boldsymbol{x}$, see equation (1), is used to compute the vertical position and the curvilinear abscissa along the track for each wheel centre. From this information, the wheel/sleeper contact force is computed. In the first step, the scalar components x_e and z_e of the distance of the wheel centre from the top surface of the nearest sleeper are computed: x_e is a stepwise linear function of the curvilinear abscissa of the centre of the wheel x_c, see Fig. 3, whilst $z_e = z_c - z_s$ with z_c and z_s the z coordinate of the wheel centre and of the upper edge of the sleeper in an x-y-z reference with x tangent to the track centreline and y parallel to the top-of-rail plane (considering track cant).

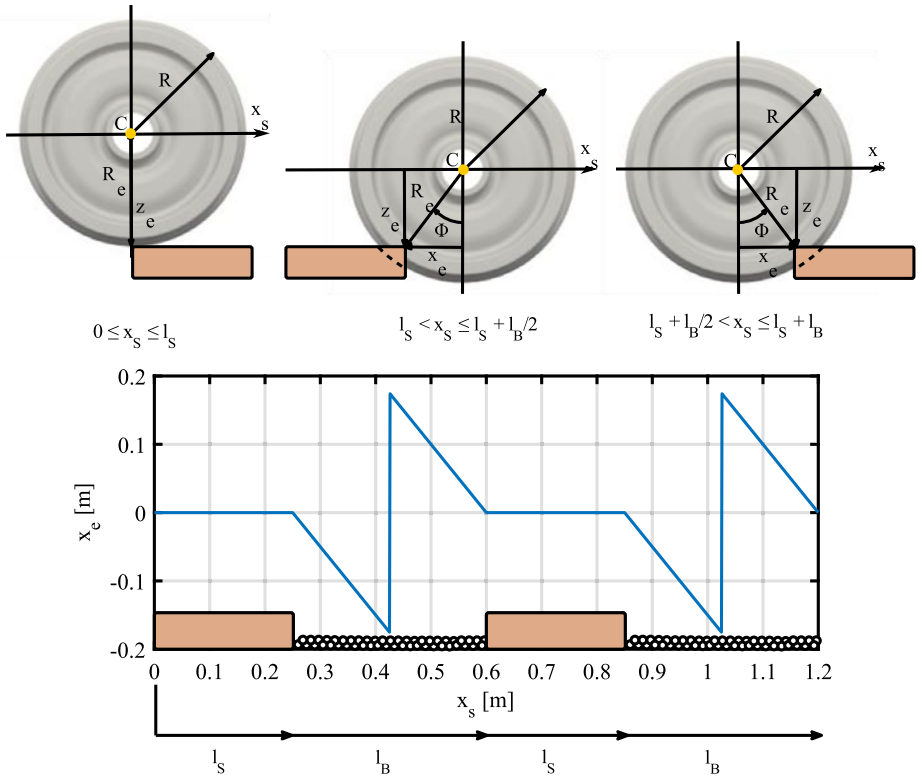

Fig. 3 Wheel–sleeper interaction model: kinematic (top) and sleeper model (bottom)

From these geometric parameters, the virtual penetration δ between the top surface of the sleeper and the wheel considered is calculated as follows:

$$\delta = R_f - \sqrt{x_e^2 + z_e^2}, \tag{7}$$

with R_f the wheel's flange radius. Due to the large curvature of the flange, the effect of the yaw angle between the two bodies on the penetration δ and then on the normal force acting on the wheel is small and can be neglected. The time-derivative $\dot{\delta}$ of the penetration is also defined as:

$$\dot{\delta} = \frac{d\delta}{dt} = -\left(\frac{x_e \dot{x}_e + z_e \dot{z}_e}{\sqrt{x_e^2 + z_e^2}}\right), \tag{8}$$

where $\dot{x}_e$ and $\dot{z}_e$ are respectively the time-derivatives of x_e and z_e.

A contact between the derailed wheel and the sleeper is detected for $\delta > 0$. The magnitude of the radial impact force component F_R on the wheel is computed according to the Lankarani–Nikravesh model [28], as defined in the following equation:

$$F_R = \begin{cases} H_c \delta^{1.5} \left(1 + \frac{3\left(1-e^2\right)}{4} \frac{\dot{\delta}}{\dot{\delta}(-)}\right), & \delta < 0, \\ 0, & \delta \leq 0, \end{cases} \tag{9}$$

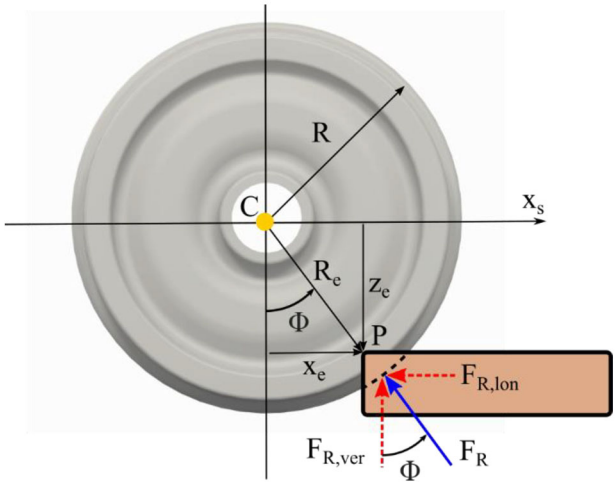

Fig. 4 Wheel–sleeper impact model – forces

where $\dot{\delta}$ is the relative approach velocity and $\dot{\delta}\,(-)$ is the relative approach velocity at the beginning of the contact. This last parameter is assumed to be equal to $\dot{\delta}$ in the time-step of the integration before the impact. The integration procedure, having an adaptive time-step, allows to accurately identify the time at which the impact starts, thus ensuring the correct estimation of $\dot{\delta}\,(-)$. The parameters used for this impact model are calibrated to have a maximum elastic interpenetration δ between the wheel flange and the upper surface of the sleeper matching the depth of the indentations found on concrete sleepers in a real derailment event reported in [17]. The derailed vehicle is an X 2000, a Swedish HS train, that has a comparable axle-load (around 17 ton) to the ETR 500, the Italian HS vehicle adopted in this work. Based on this analysis, the parameters used in the Lankarani–Nikravesh impact model are $H_c = 1.6\text{e}8\ \text{N/m}^{1.5}$ and $e = 0.5$.

Finally, as shown in Fig. 4, knowing the position of the impact point P on the surface of the wheel flange and assuming that the impact force is normal to the wheel surface, it is possible to compute the impact angle Φ with respect to the centre of the wheel and decompose the impact radial force into vertical and longitudinal components that are applied to the considered wheelset.

3.2 Wheel–ballast interaction model

Modelling the interaction between a derailed wheel and the ballast is still an open research topic, which has been so far addressed only by a limited number of researchers [14, 15]. In this paper, a new approach is proposed based on terramechanics models.

It must be noted that these models may require high computation effort: for this reason, in this work, terramechanics models are not introduced directly in the multi-body model. Instead, a detailed model considering a single wheel in contact with the ballast modelled as a soft soil is used to generate a look-up table, which is then interpolated at each time step of the numerical simulation. The model used to describe the wheel–ballast interaction is based on two fundamental relations used in terramechanics: the semi-empirical pressure–sinkage relationship known as the Bekker model [19] and the relationship between stress and shear displacement from the Janosi–Hanamoto model [20]. These two models are used to define respectively normal and tangential stresses at the interface between the derailed wheel and the ballast.

According to this approach, the wheel–ballast interaction results in a force that depends on the wheel's geometry, position and velocity relative to the soil. In this way, for a given geometry of the wheel, it is possible to pre-compute and store in the look-up table the contact forces for a given range of states of the wheel.

3.2.1 The pressure–sinkage Bekker model

The semi-empirical pressure–sinkage model adopted in this paper comes from the work by Bekker [19], in which a connection is established between the displacement (sinkage, s) and the stress (pressure, σ) experienced by a small rectangular portion of a solid surface in contact with a soft terrain:

$$\sigma = ks^n = \left(\frac{k_c}{b} + k_\phi\right) s^n, \tag{10}$$

where:

- s [m] is the sinkage;
- σ [N/m^2] is the normal pressure;
- b [m] represents the smallest dimension of the rectangular section;
- n [-] is the sinkage index, a non-dimensional coefficient depending on the type of soft terrain considered;
- k_c [kPa/m^{n-1}] is a coefficient depending on the cohesion of the terrain material;
- k_ϕ [kPa/m^n] is a coefficient depending on the angle of internal friction of the terrain material.

This model is adopted to locally describe the contact between the wheel and the ballast: the wheel's surface is discretized into a grid of rectangular cells, and the Bekker model is applied to each cell separately. This allows to obtain the region of the wheel surface in contact with the ballast and the contact pressure at each cell belonging to the contact region. The resulting wheel/ballast force is then obtained through vector summation over all cells in the contact region.

In equation (10), parameters n, k_c and k_ϕ are usually determined from field tests. References [29, 30] provide the results of several compression tests, called plate load tests: these results are used in this work to estimate the aforementioned parameters.

Following the approach presented in reference [31], a residual function F is introduced, see equation (11), in which σ_i and s_i are the pressure and sinkage values from the ith measurement in the test and m is the number of measurements in the test. To consider the exponential nature of equation (10), the residual function considers the logarithms of the measured pressure and sinkage values and consists of a weighted sum of the squares of the difference between the measured data and the interpolating function from equation (10), using the squared pressures as the weights of the sum and assuming that all experimental observations taken into consideration hold equal reliability with respect to the measuring errors.

$$F = \sum_{i=1}^{m} \sigma_i^2 \left(\ln \sigma_i - \ln k - n \ln s_i\right)^2 \tag{11}$$

The identification of the coefficients in equation (10) was performed in two steps. First, the coefficients n and k were identified separately for the experimental data from references [29] and [30]. Then, a common value of the sinkage index n was obtained as the average of

Table 1 Fitting parameters for the pressure–sinkage model

Exp. data from:	Plate width [m]	Plate length [m]	n_1 [−]	k_1 [kPa/m^n]	n_{avg} [−]	k_{corr} [kPa/m^n]
[29]	0.08	0.08	2.15	2.29E + 10	1.92	4.26E + 09
[30]	0.30	0.30	1.68	2.95E + 08	1.92	2.02E + 09

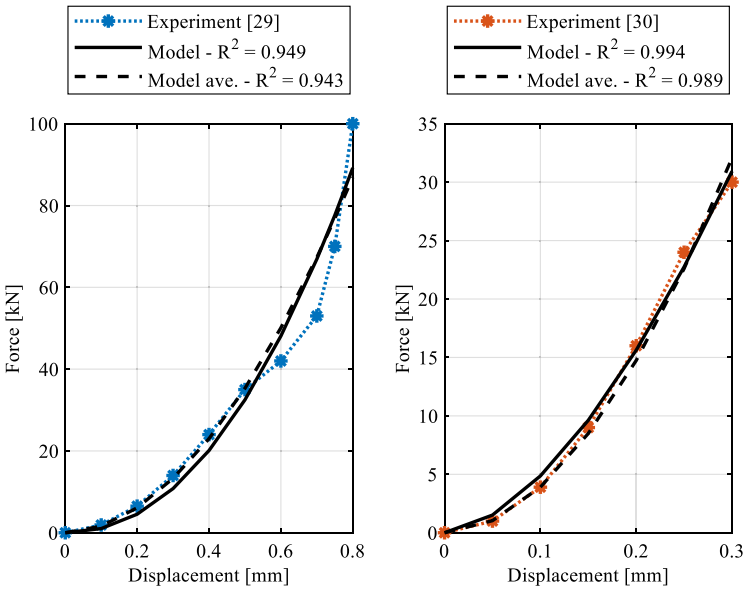

Fig. 5 Comparison of the measured and computed force–sinkage curves for plate load tests published in [29] and [30]

the two values obtained in the first step of the parameter identification procedure, and the experimental data were refitted for the averaged sinkage value iterating the identification of the coefficient k. Finally, from the two values of coefficient k identified in the second stage for two different sizes of the plate used in the experiment, the values of parameters k_c and k_ϕ were obtained according to equation (10).

The values n_1 and k_1 of the parameters identified in the first stage of the identification, the averaged sinkage coefficient n_{avg} and the corrected k_{corr} coefficients identified in the second stage are reported in Table 1 for the two experiments.

Figure 5 shows the results of the fitting procedure for the experiments reported in the two references in terms of the force–sinkage relationship. The dots represent the experimental values taken from the two references, the dashed line the model from equation (10) identified in the first stage (i.e. using two different values of the sinkage index for the two experiments) and the solid line the model from the same equation using the coefficients identified in the second stage (using the averaged sinkage coefficients). Both models show a good match to the experimental data for both experiments, and the difference between the two models is small. The legend of the two plots also reports the R^2 coefficient of determination, which are in all cases close to 1, confirming that, after parameter identification, the model represented by equation (10) provides an accurate prediction of both sets of experimental data. From the k_{corr} coefficients obtained and considering the size of the plate used

in the two experiments, the following values were obtained for the two coefficients k_c and k_ϕ: $k_c = 2.24 \cdot 10^8$ kPa/m^{n-1} and $k_\phi = 1.27 \cdot 10^9$ kPa/m^n.

3.2.2 Stress–shear displacement relationship from the Janosi–Hanamoto model

The tangential stresses are calculated according to [20]. The stress–displacement relationship in tangential direction is described by the Mohr–Coulomb theory according to the implementation by Janosi and Hanamoto to take into account the influence of the shear displacement, resulting in equation (12):

$$\begin{aligned} \tau(\theta) &= \tau_{max} \cdot \left(1 - e^{-d(\theta)/K}\right) \\ \tau_{max} &= c + sin(\phi) \cdot \sigma(\theta), \end{aligned} \tag{12}$$

where:

- τ is the shear stress;
- d is the shear displacement (slip);
- τ_{max} is the maximum value of shear stress;
- K is the shear deformation parameter of the material;
- c is the cohesion (or adhesion) coefficient;
- ϕ is the internal friction angle of the material;
- σ is the normal stress from equation (10);
- θ is the contact angle of the infinitesimal area considered;

The values of the parameters of this model are obtained from the results of experimental tests on ballast presented in [32]. Since this reference highlights the limitations of laboratory shear tests in view of ballast characterization, only the results from full-scale tests, presented in the same paper, have been used for the identification of the parameters of the Janosi–Hanamoto model.

Like for the sinkage–pressure model, parameter identification for the shear model is performed in two steps. Initially, each ith experiment is fitted to minimise the quadratic error, resulting in the determination of K_i and τ_{max_i}. Then, the value $K = 0.009$ m for the material is obtained by averaging the K_i values from the different tests and the measurements are fitted again, considering the average value of coefficient K, to obtain the final value of coefficient τ_{max}.

As a result, through a linear interpolation shown in Fig. 6 the values $c = 1.218$ kPa and $\phi = 46.62°$ are computed, completing the parameters estimation process for the stress–shear displacement model.

3.2.3 Contact table generation

The model of normal and shear stresses is used to derive the look-up tables used in the multi-body simulation to consider the contact between a derailed wheelset and the ballast. The creation of the look-up table is performed considering the 3D surface of the wheel discretized into 26,700 rectangular elements, see Fig. 7. Different kinematic states of the wheel are considered, each one described by a specific combination of the following parameters, shown in Fig. 8:

- wheel centre sinkage s_C;
- longitudinal velocity v of the wheel centre;

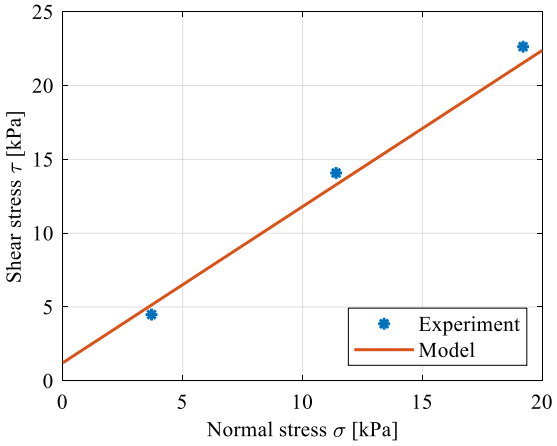

Fig. 6 Parameter fitting for the shear stress model

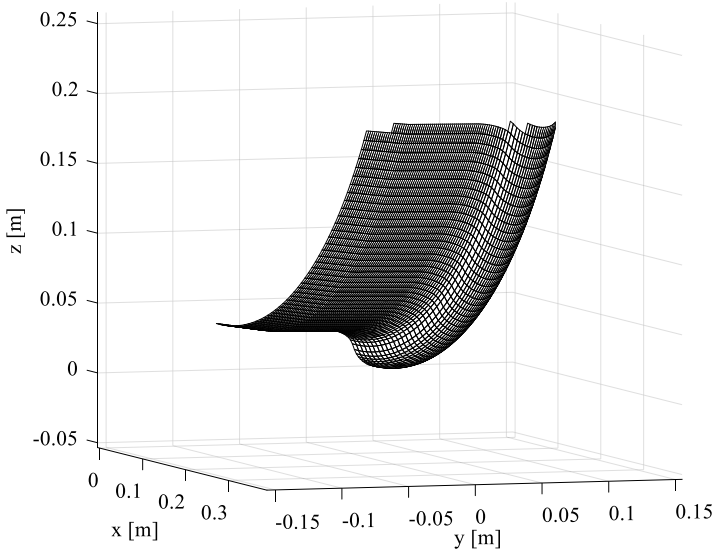

Fig. 7 Discretization of the wheel surface for the generation of the contact tables

- angular speed of the wheel ω.

For each condition, the sinkage, sliding speed and contact angle are computed at the centre of each cell. Then, the normal and shear stresses are computed at each cell using equations (10) and (12) respectively, and finally the resulting longitudinal and vertical contact forces (F_x and F_z) and the moment of shear forces M_y, see Fig. 8, are obtained from the summation of contributions from all cells in contact with the ballast and stored in the look-up table.

The slip d_i at the ith cell of the discretised wheel surface is obtained from the integration of the sliding speed $v_{s,i}$ for the same cell defined as follows:

$$v_{s,i} = R_i\omega - v cos\,(\theta_i)\,, \tag{13}$$

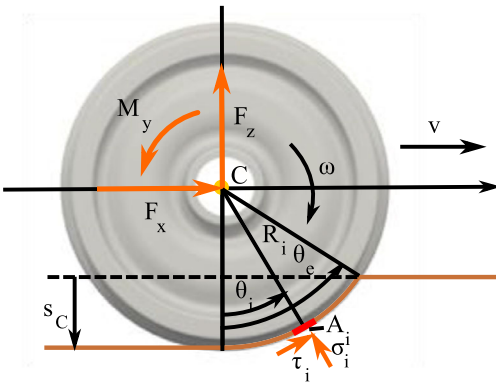

Fig. 8 Kinematic parameters s_C, v and ω and output variables F_x, F_z, M_y considered in the construction of the look-up tables of wheel/ballast forces (the horizontal brown line shows the upper surface of the ballast)

where R_i and θ_i are respectively the distance from the wheel centre and the angular position of the centre of the ith cell, see Fig. 8. To obtain the slip at the ith cell, the sliding speed from equation (13) is integrated in time from $t = 0$ corresponding to the time when the ith cell initially comes in contact with the ballast to $t = t_i$ when the centre of the cell is located at angle θ_i:

$$d_i = R_i \int_0^{t_i} \omega \left[1 - \frac{v}{R_i \omega} cos\,(\theta)\right] dt. \tag{14}$$

Noting that $\omega\, dt = -d\theta$ and that at time $t = 0$ the angular position of the cell is the entry angle θ_e (see Fig. 8), the above expression is re-written as

$$\begin{aligned} d_i &= R_i \int_{\theta_e}^{\theta_i} -\left[1 - \frac{v}{R_i \omega} cos\,(\theta)\right] d\theta \\ &= R_i \int_{\theta_i}^{\theta_e} \left[1 - \frac{v}{R_i \omega} cos\,(\theta)\right] d\theta \\ &= R_i \left\{(\theta_e - \theta_i) - \frac{v}{R_i \omega} \left[sin\,(\theta_e) - sin\,(\theta_i)\right]\right\}. \end{aligned} \tag{15}$$

The final expression in equation (15) allows to compute the slip at the ith cell as function of the ratio v/ω and of the parameters R_i and θ_i, which are derived from the wheel center sinkage s_C and from the discretization of the wheel surface. It should be noted that equation (15) assumes that the angular speed of the wheelset remains constant while the ith cell flows from the entry position θ_e to the present position θ_i. This assumption is acceptable considering that even for the largest sinkage and lowest angular speed considered in the look-up table, 0.1 m and 154 rad/s respectively, the time taken by the ith cell to move from the entry position to the present position is approximately 4 milliseconds, so in this short time the deceleration of the wheel can be considered negligible. The range of values to be considered for the three entries of the look-up table s_c, v and ω was defined and validated through iterative trials, making sure that all kinematic conditions encountered in the simulations are covered.

The final ranges chosen are:

- Sinkage of the wheel centre s_c: $0 - 0.1$ m, in steps of 0.005 m;

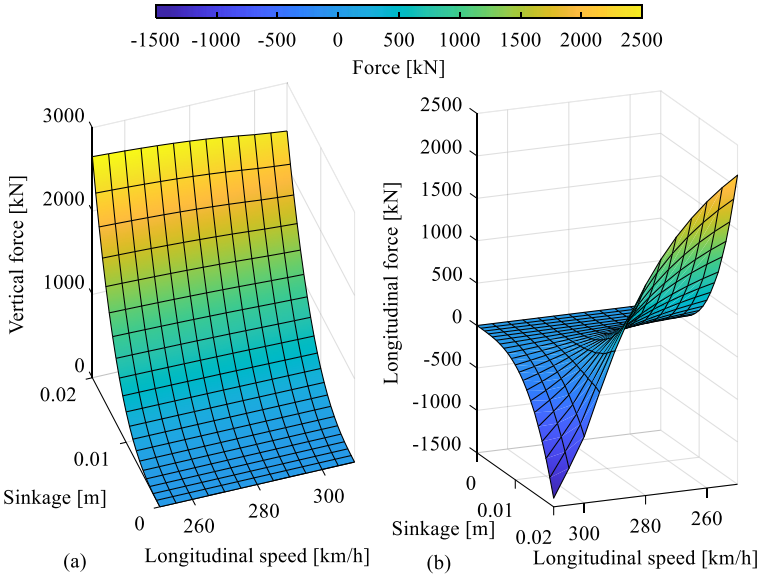

Fig. 9 Vertical force (a) and longitudinal force (b) for $\omega = 170$ rad/s ($\omega R = 275$ km/h with R the nominal radius of the wheel)

- Wheel centre speed v: $69.4 - 86.1$ m/s (or $250 - 310$ km/h), in steps of 1.4 m/s (or 5 km/h);
- Wheel angular speed ω: $154.3 - 191.4$ rad/s, in steps of 3.1 rad/s.

Note that the values chosen for the angular speed correspond to a peripheral speed of the wheel ωR in the range 250 – 310 km/h, with $R = 0.45$ m the nominal radius of the wheel.

Figure 9.a and Fig. 9.b show, as an example, the longitudinal and vertical forces for different combinations of wheel centre sinkage and longitudinal speed and for a fixed value of the angular speed corresponding to a peripheral speed of the wheel surface equal to 275 km/h. The vertical force component is mostly affected by wheel centre sinkage and is only weakly affected by the sliding of the wheel surface over the ballast. The longitudinal force is, instead, strongly affected by the ratio of the wheel centre speed and peripheral speed, as expected, and negative/positive values of this force are obtained respectively when the ratio $v/\omega R$ is above/below the unit value.

4 Results

4.1 Simulation of a derailment test and comparison with measurements

The simulation of the post-derailment behaviour of a railway vehicle is inherently affected by uncertainties related to the modelling of the interaction between the derailed wheels and the railway infrastructure, so it is important to assess the accuracy of the model, if possible comparing the outputs of the model with experimental results. In this section, derailment tests performed on a freight wagon and published in [13] are reproduced using the multibody model of a single freight wagon and the model of wheel–sleeper and wheel–ballast

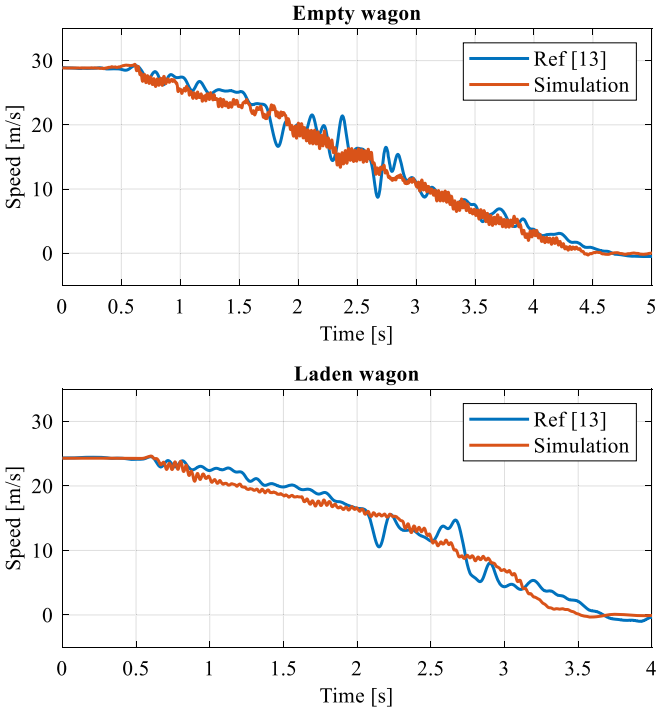

Fig. 10 Simulation of the derailment of a freight wagon and comparison with measurements

interaction described in Sect. 3. The tests (described in the reference as "full wagon derailment tests") were performed with a locomotive pushing the wagon along the track until the axles of the wagon encounter a derailment device, which forces both wheels of the axle to climb the flange and fall aside the rail. The locomotive and wagon are not coupled and not in contact when the wagon reaches the derailment device, so it is possible to consider the wagon as isolated from the locomotive. The test was repeated with the wagon in tare and laden conditions, and in both cases the speed of the vehicle was recorded until the wagon reached a stop.

To simulate this experiment, a model of the freight wagon was defined using the data published in [13] and standard data for the Y25 bogie. In this model, the mass of the vehicle body is chosen to match the weight of the wagon in tare and laden condition as stated in the reference, and ORE S1002 wheel profiles are assumed. To simulate this case, a specific look-up table was generated according to the method described in Sect. 3.2.3, considering the parameters of the freight wagon and a range of linear/angular speed of the wheel consistent with the derailment experiment.

In the numerical simulation, the initial speed of the wagon is set to the same value recorded in the two tests published in the reference (in both tests, the initial speed of the wagon when approaching the derailment device was slightly lower than 30 km/h) and a modified wheel/rail contact table was created to account for the effect of the derailment device.

Figure 10 compares the measured and simulated time history of the vehicle speed for the wagon in tare condition (upper plot) and in laden condition (lower plot). In both cases, the speed profile obtained from the simulation matches well the experimental result, although

Table 2 Comparison between experimental and numerical results for the derailed wagon

		Experimental	Numerical	Deviation
Empty wagon	Time to stop	4.91 s	4.53 s	7.9%
	Travelled distance	21.0 m	20.6 m	2.2%
Laden wagon	Time to stop	3.62 s	3.56 s	1.6%
	Travelled distance	15.9 m	15.4 m	3.1%

the measured speed profile shows some oscillations not reproduced by the mathematical model. Furthermore, the results of the simulation and the measurements from the experiment are in very good agreement in terms of the total duration of the motion of the wagon before coming to a stop and of the distance travelled after the derailment, see the comparison presented in Table 2. For both the experimental and numerical results, the stopping time was computed applying a 1 s moving average to the speed signal to remove the high-frequency fluctuations and then computing the distance in time between the first occurrence of a speed value lower than 99.5% of the initial speed until reaching 0.5% of the initial speed.

Despite the limitations inherent to this comparison, it can be concluded that the wheel–sleeper and wheel–ballast interaction models defined in this work allow a realistic description of the resistance to motion encountered by the wheels after the derailment.

4.2 Derailment of a high-speed locomotive and impact with the DCW

The model described in Sects. 2 and 3 is applied to the study of a derailment scenario considering a high-speed ETR-500 class locomotive running at 300 km/h along a curve with radius 5,450 m and superelevation 120 mm. This scenario was identified in agreement with experts from RFI (the Italian infrastructure manager) as particularly relevant to the structural sizing of the DCW. Figure 11 (left) shows a top view of the curve and of the DCW (red line), which runs parallel to the track in the curve. As described in Sect. 2, an FE model of the DCW is introduced to consider the flexibility of this structure in the impact with the derailed train. In more detail, a portion of the DCW having length 80 m is modelled, which is sufficient to consider the impact with the derailed train. In the FE model, the curvature of the DCW is neglected considering that the radius of the curve is two orders of magnitude larger than the length of the DCW interested by the impact with the vehicle. Figure 11 (right) qualitatively shows the FEM model of the DCW, which is composed by 4-node rectangular Kirchoff plate elements. Each element has a length in longitudinal direction of 1 m and a height in vertical direction of 0.55 m, and the plate elements are arranged in three rows, resulting in 240 plate elements and 324 nodes of which 81, representing the base of the DCW, are clamped to the ground. The main geometric data and material properties of the DCW are summarised in the Appendix. As shown in Fig. 12, the DCW is designed to contact the axle-boxes of the derailed wheelset and its height h_w is such that a contact with the car body is not possible.

The derailment scenario considered assumes the failure of one journal in the trailing wheelset of the front bogie, taking place while the vehicle negotiates the constant-radius portion of the curve. This is a realistic, although fortunately very rare scenario, as axle failure may occur due to the notch effect at the transition between the journal and the wheel seat in the axle. The failure is simulated by suddenly setting to zero the force transmitted by the corresponding primary suspension causing the sudden unloading of the inner wheel of the

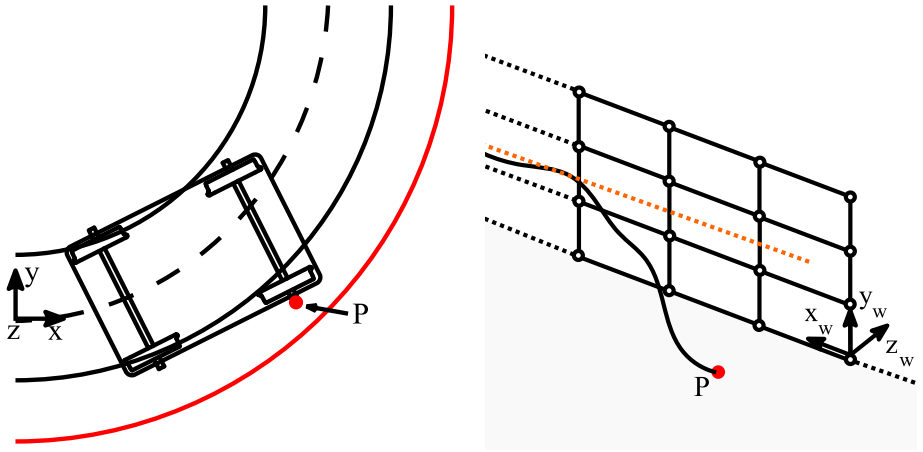

Fig. 11 Left: Top view of the front bogie and the derailment containment wall (in red) in the curved section. Right: 3-meter portion of FEM of the deformable structure. In both sub-figures the position of a candidate impact point P is shown

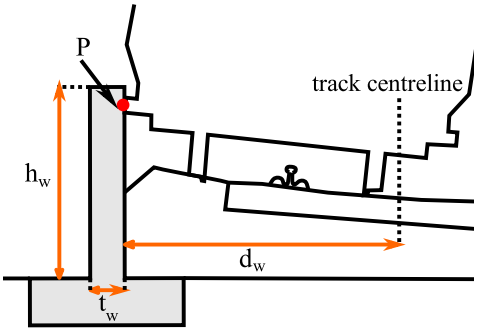

Fig. 12 Side-view of the DCW (in grey) with highlighted potential contact point P. With orange lines are reported the parameters defining the DCW

trailing axle and, due to the redistribution of the vertical forces in the primary suspension, the unloading of the outer wheel of the leading axle, which climbs the rail. This leads eventually to the derailment of the front bogie and then to the impact of the leading wheelset of the same bogie with the DCW. More details about the derailment process are provided in [18].

The derailment phase of the front bogie is described in [18] and is not repeated here for the sake of brevity, while in this section the focus is on the effect of the sleepers and ballast on the post-derailment phase and on the impact with the DCW.

Figure 13 shows the vertical dynamics of the four wheels of the first bogie, starting from the failure of the journal. The abscissa of the plots is the distance travelled by the vehicle after the failure. The vertical forces (values shown on the y axis to the left) are plotted in three different colours, indicating the different type of possible contact: blue lines for wheel–rail contact, red for wheel–sleeper contact and yellow for wheel–ballast contact. The dashed line in each plot shows the vertical position of the wheel's contact point relative to the top of the rail (TOR), the value of this quantity is shown on the y axis to the right.

The derailment of the leading wheelset occurs approximately 50 m after the failure of the journal and can be noticed from the sudden drop in the vertical position of the two wheels. The inner wheel of this wheelset falls between the two rails, so it is impacting only the

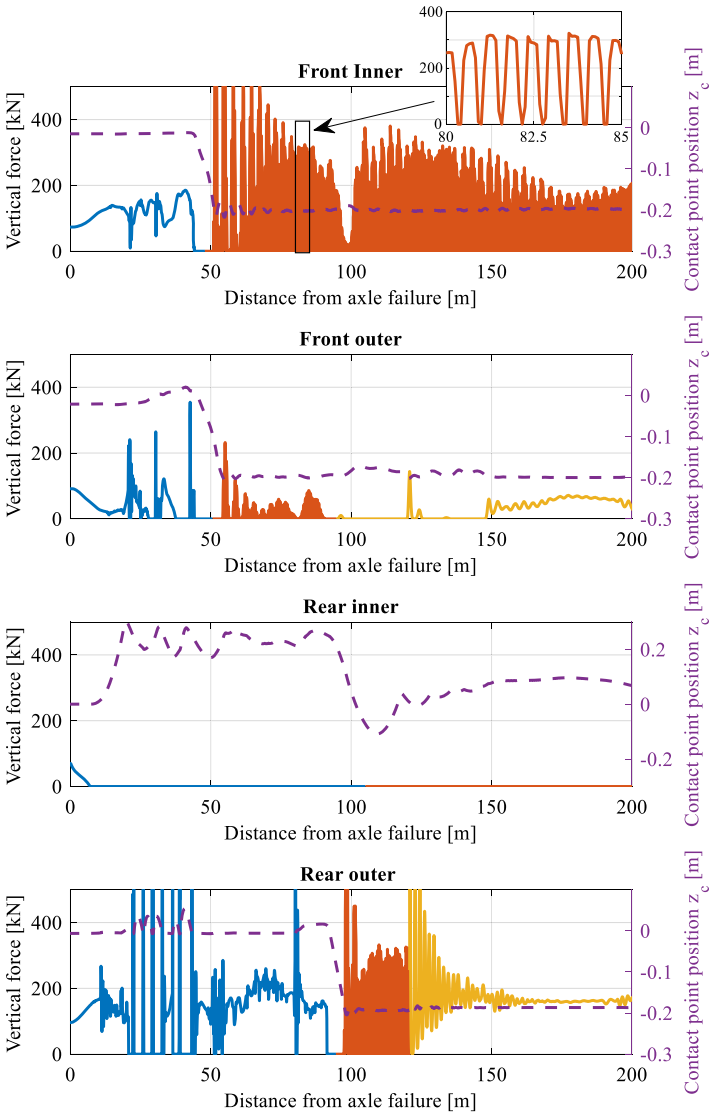

Fig. 13 Vertical force acting on the four wheels of the front bogie and vertical position of the contact point with respect to the top of rail (TOR). The forces are represented with different colours depending on impact-contact type: blue for wheel–rail contact, red for contact with sleepers, yellow for contact with ballast

sleepers (red line for the vertical forces). The spatial frequency of the peaks corresponds to the spacing between the sleepers, as shown in the detail of the time history shown in the upper right corner of the plot. After the vehicle has travelled 90 m approximately, the vertical force swiftly goes down to zero, denoting a short-duration loss of contact with the rail: this happens because the second wheelset is derailing, and this also affects the dynamics of the first wheelset.

It should be noted that while the derailed wheel impacts the sleepers, the peak values of the contact force may be significantly affected by the tolerances of the numerical method

used for the integration of the equations of motion. A sensitivity analysis was therefore performed, varying the absolute and relative tolerances of the numerical method in the ranges 1E-6÷1E-7 and 1E-3÷1E-5 respectively: the largest difference found for the maximum impact force with the sleeper is less than 3% of the average of the peak forces obtained in all the cases of the sensitivity analysis. Hence, it is concluded that the model has sufficient numerical robustness.

The outer wheel of the leading wheelset, after falling down from the rail, impacts the sleepers and progressively moves away from the track until contact with the ballast starts to take place. The transition from the contact with the sleepers to the contact with the ballast takes place when the wheelset has travelled approximately 100 m after the failure of the journal.

In the trailing wheelset, the failure of the journal causes a sudden decrease of the vertical force on the inner wheel because the vertical force transmitted across the primary suspension vanishes suddenly. As a consequence, after a short transient, the wheel lifts up from the rail until it contacts the gearbox. The contact of the lifted wheel with the gearbox is modelled by means of a stiff contact element with a dead zone whose width is estimated from the drawings of the bogie. It can be noted that after lifting up by 0.23 m approximately, the wheel remains at a fairly constant height due to the contact with the gearbox, before moving down in the final part of the simulation (distance from axle failure $>$ 100 m), but never getting back in contact with the rail or with any other part of the infrastructure. The outer wheel of the trailing wheelset derails when the vehicle has travelled approximately 90 m after the failure, then impacts the sleepers and finally gets in contact with the ballast.

Figure 14 shows the radial motion of the centre of mass of the two wheelsets (dotted lines) and of the two external axle boxes (solid lines), identified as control points at which an impact with the DCW may occur. The black solid lines show the position of the rails and the undeformed position of the DCW, while the dashed black line shows the position of the track centreline. Following the derailment event, both the leading and trailing wheelsets (respectively blue and red lines) move outside the curve and towards the DCW. The control point on the leading wheelset (solid blue line) impacts the DCW after a travelled distance of approximately 135 m from the axle failure, and after the first impact it remains in contact with the structure.

Figure 15 shows the variation of the kinetic energy of the vehicle during the derailment event, a zoom-in of the first 20 m is shown in the upper right corner of the figure. The variation of the kinetic energy of the vehicle is computed with respect to the initial state of the vehicle when the failure of the journal occurs and the simulation assumes no traction or braking is applied to the wheels. Initially, a very small increase of kinetic energy is observed due to the release of the elastic energy stored in the primary suspension following the axle failure. Then, the kinetic energy starts decreasing although the initial trend is not monotonic due to some exchange between kinetic energy and potential energy in the suspensions of the vehicle. After approximately 50 m the leading wheelset derails, and the same happens to the trailing wheelset approximately around 90 m from the axle failure. These two events cause a slight increase in the kinetic energy of the vehicle because the leading/trailing wheelset is falling from the rails after derailment, transforming part of gravitational potential energy into kinetic energy. Once the two wheelsets are derailed, the trend of kinetic energy becomes monotonically decreasing due to the large resistance to motion encountered by the derailed wheels.

After interacting with the sleepers and the ballast, the outer axlebox of the leading wheelset impacts with the DCW. The spatial position of the FE model of the DCW is defined so that the first impact with the vehicle happens at a distance of 10 m from the rearmost

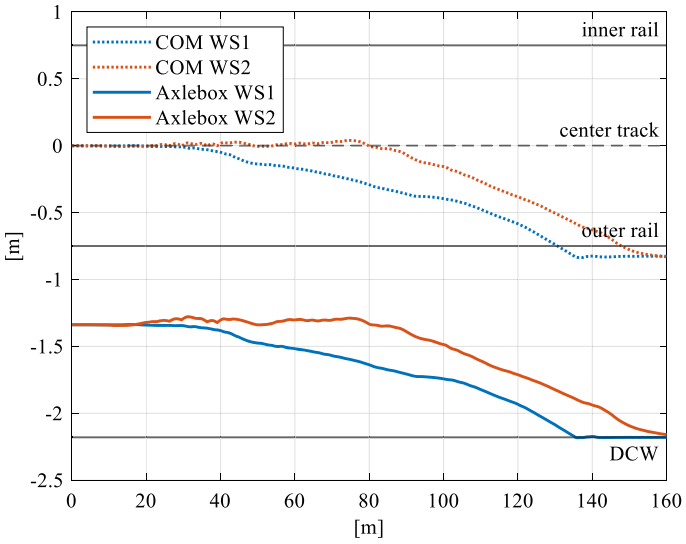

Fig. 14 Position of the centre of mass (COM, dashed lines) and of the axle boxes (solid lines) respectively of the wheelsets 1 and 2 of the front bogie

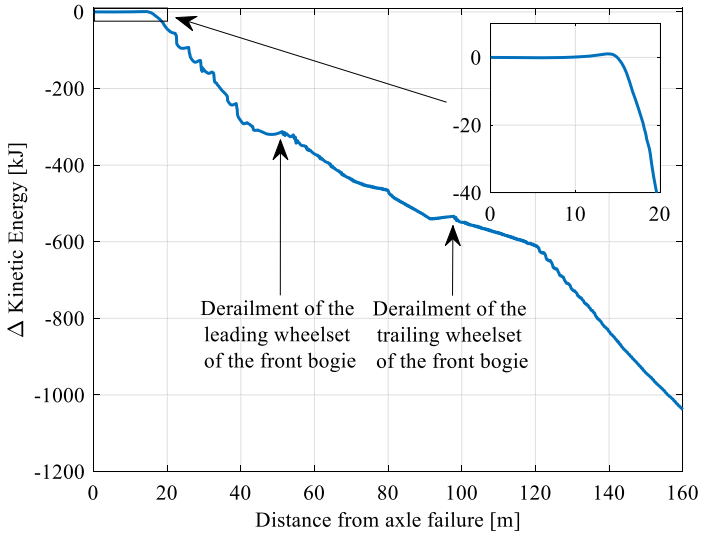

Fig. 15 Variation of the kinetic energy of the vehicle versus the distance from axle failure

end of the model, to reduce the effect of the model's boundary conditions on the simulation of the impact. Figure 16 shows the normal component of the impact force in the reference frame of the DCW. From this figure it is clear that the maximum impact force is developed during the initial phase of the impact, as this is the phase of the impact corresponding to the largest kinetic energy of the vehicle.

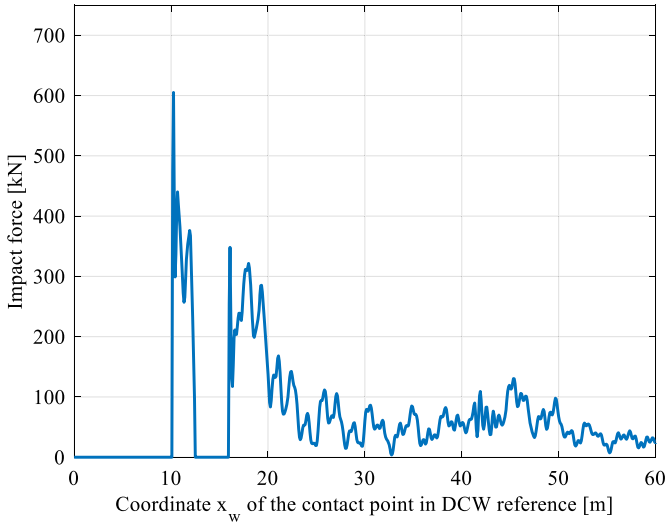

Fig. 16 Normal force between the axle-box of the first wheelset and the DCW

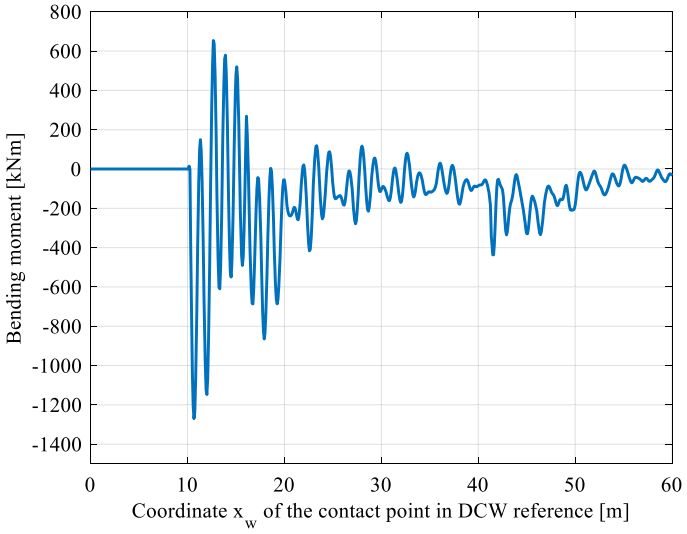

Fig. 17 Integral of the bending moment at the base of the DCW

Figure 17 shows the bending moment at the base of the DCW produced by the impact on the overall length of the structure, computed as expressed in equation (6) and plotted vs the x_w coordinate of the contact point. As expected, the maximum value of the bending moment takes place shortly after the maximum value of the impact force and then a fast oscillatory motion of the impacted wall can be noted.

To highlight the effect of the model of the interaction between the derailed vehicle and the sleepers and ballast, some results from the simulation presented above are compared in

Table 3 Comparison between derailment simulation without ballast and sleepers [18] and the present work

Data	Simplified model of the post-derailment phase [18]	Detailed model of the post-derailment phase (this paper)
Maximum impact force [kN]	435	605
Maximum bending moment [kNm]	886	1269
Impact time after axlebox failure [s]	2.3	1.7
Impact speed [m/s]	0.95	1.45
Leading bogie yaw angle [rad]	0.012	0.077

Table 3 to the ones presented in [18], where the same scenario was simulated considering the derailed wheels in contact with a rigid horizontal plane.

This comparison allows to point out the effect of the more accurate modelling of the post-derailment motion of the vehicle enabled by the models of the sleepers and ballast introduced in this paper.

The values compared in Table 3 show that the simulation results are highly sensitive to the model used to represent the interaction between the derailed vehicle and the railway infrastructure and that simplifying the railway infrastructure to a rigid plane (as done in [18] and also in several other papers) results in severely underestimating the peak impact force and the maximum bending moment in the DCW.

This happens primarily because the ballast has the effect of rotating the derailed bogie around its vertical axis (yaw rotation). In fact, when a wheel starts interacting with the ballast, it encounters a resistance force that generates a yaw moment on the wheelset and, through the primary suspensions, to the frame of the derailed bogie. In this way, the vehicle is impacting the DCW with a less favourable angle. Moreover, the yaw rotation of the bogie causes the vehicle to impact earlier the DCW. Therefore, the impact speed (component normal to the DCW of the bogie velocity vector at the impacting point) is larger when the effect of the sleepers and the ballast effect are considered in detail, leading to a higher impact force transferred to the DCW during the impact.

The computational effort required to run the simulation case presented above is 3,138 s (less than an hour) on an Intel® Core™ i7-8750H Processor with 2.20 GHz. This effort refers to a simulated time of 18 s, covering the entire derailment process starting with the vehicle approaching the curve and negotiating the entry transition until reaching the full-curve section, then undergoing the derailment and finally impacting the DCW.

5 Conclusion

This paper presents a model of the dynamics of a derailed railway vehicle with focus on the interaction of the derailed wheels with the sleepers and the ballast, and the subsequent impact with a deformable containment structure.

A contact–impact management algorithm is introduced to consider the interaction of the derailed vehicle with different components of the railway infrastructure, namely the sleepers and the ballast.

A detailed model of the impact of the derailed wheels with the sleepers is introduced, treating the sleepers as a periodic profile causing inelastic impacts with the wheels, according to the Lankarani–Nikravesh model of impacts between solid bodies. In this model, the

flexibility of sleeper support is presently neglected, but the inclusion of this effect is envisaged as a possible future extension of the model.

The model of the interaction between the derailed wheels and the ballast consists of a non-linear pressure–sinkage relationship used to compute the local normal pressure between the ballast and the wheel, and of a shear stress–displacement relationship used to compute the local shear stresses on the wheel. This local model is applied cell-wise to a fine discretisation of the wheel outer surface and is used to derive look-up tables defining the resulting forces applied by the ballast on the wheel for a range of kinematic states of the wheel. The look-up table is then used in the numerical simulation of the multi-body model describing the post-derailment dynamics of the complete railway vehicle.

The results of a comparison with experimental results concerning a derailment test performed on a single freight wagon show good agreement, confirming the appropriateness of the approach developed to consider the interaction of the derailed wheels with the railway infrastructure.

Next, the model is applied to study the derailment of an HS vehicle travelling at 300 km/h in a curve and suffering the mechanical failure of one axle journal, causing the front bogie of the vehicle to derail and then impact the containment wall.

The comparison of the results obtained using the model presented in this paper and an earlier model not considering the interaction of the derailed wheels with the sleepers and the ballast shows that the forces resulting from the interaction with the ballast and the sleepers have a large effect on the dynamics of a derailed bogie. In particular, due to the longitudinal forces exchanged with the ballast on the outer derailed wheels, the front bogie rotates around its vertical axis towards the containment structure. This leads to impacting the DCW with a less favourable angle, thereby leading to higher peaks of both the impact force and the bending moment at the base of the DCW.

It should be noted that the maximum bending moment is a key input to the structural sizing of the DCW and, therefore, the results obtained suggest that a sufficiently accurate model of the forces caused by the interaction between the derailed vehicle and the sleepers and ballast is pivotal to the use of multi-body simulation tools to support the development and design of infrastructure-based devices intended to mitigate the effects of train derailments.

Appendix

Table 4 Geometrical data and material data of the derailment containment wall

Data	Symbol	Value	Units
Geometric data			
Height	h_w	1650	mm
Thickness	t_w	300	mm
Distance from track centreline	d_w	2180	mm
Material data: reinforced concrete C30/37			
Density	ρ	2500	kg/m^3
Young's module	E	3.28E10	N/m^2
Poisson's ratio	ν	0.2	–

Nomenclature

b	Smallest dimension of the interaction surface in the pressure–sinkage model
c	Cohesion coefficient
d	Shear displacement
d_i	Slip of the ith element
d_w	Radial distance of the DCW from the track centreline
e	Coefficient of restitution
h_w	Height of the DCW
k	Coefficient of the pressure–sinkage model
k_c	Pressure–sinkage coefficient depending on the cohesion
k_ϕ	Pressure–sinkage coefficient depending on the internal friction
l_k	Horizontal length of the kth finite element in the DCW model
m	Number of measurements used for the calibration of the pressure–sinkage model
n	Sinkage index
s	Sinkage
s_c	Wheel center sinkage
t	Thickness of the plate
t_w	Thickness of the DCW
v	Wheel longitudinal speed
$v_{s,i}$	Sliding speed at the ith cell of the wheel surface
w	Bending displacement of the plate
x_c	Curvilinear abscissa of the wheel centre
x_e	Horizontal distance of the wheel centre from the sleeper
x_w	Longitudinal position of the contact point between the axle box and the DCW
z_c	Vertical position of the wheel centre
z_e	Vertical distance of the wheel centre from the sleeper
D	Flexural rigidity of the plate
E	Young's modulus of the material of the DCW
F	Residual function for the calibration of the pressure–sinkage model
F_x	Horizontal component of the wheel/ballast force
F_z	Vertical component of the wheel/ballast force
F_R	Radial wheel-sleeper force
H_c	Hertzian stiffness
K	Shear deformation parameter
M_{tot}	Total bending moment at the base of the DCW
M_y	Moment of the shear forces between wheel and ballast
$M_{y,k}$	Bending moment around the y-axis of the kth plate element
R_f	Radius of the wheel's flange
R_i	Wheel radius at the ith cell of the wheel surface
σ	Normal pressure
δ	Virtual penetration between wheel and sleeper
$\dot{\delta}$	Relative approach velocity
$\dot{\delta}(-)$	Relative approach velocity before impact
θ	Contact angle
θ_e	Entry angle
θ_i	Angular position of the ith cell of the wheel surface
ν	Poisson's ratio of the material of the DCW
ρ	Material density of the DCW
τ	Shear stress

τ_{max}	Maximum shear stress
ϕ	Internal friction angle
ω	Wheel angular speed
Φ	Impact angle
$\boldsymbol{x}$	Vector of independent coordinates of the vehicle
$\boldsymbol{x}_s$	Vector of independent coordinates of the DCW
$\boldsymbol{x}_{s,k}$	Vector of nodal displacements for the kth plate element
$\boldsymbol{K}_s$	Stiffness matrix of the DCW
$\boldsymbol{M}$	Mass matrix of the vehicle
$\boldsymbol{M}_s$	Mass matrix of the DCW
$\boldsymbol{Q}_v$	Vector of inertia forces that are quadratic in velocity
$\boldsymbol{Q}$	Vector of generalised forces acting on the vehicle
$\boldsymbol{Q}_s$	Vector of generalised suspension components
$\boldsymbol{Q}_g$	Vector of generalised weight forces
$\boldsymbol{Q}_c$	Vector of generalised wheel–rail contact forces
$\boldsymbol{Q}_{w-s}$	Vector of generalised wheel–sleeper contact forces
$\boldsymbol{Q}_{w-b}$	Vector of generalised wheel–ballast contact forces
$\boldsymbol{Q}_{i,v}$	Vector of generalised impact forces on the vehicle
$\boldsymbol{Q}_{i,s}$	Vector of generalised impact forces on the DCW
$\boldsymbol{R}_s$	Damping matrix of the DCW
$\boldsymbol{\phi}_k$	Shape function's vector for the kth plate element

Author contributions M.S, F.M., and R.R. developed the numerical model and performed the calculations and numerical simulations. M.S., F.M., E.D.G., and S.B. wrote the manuscript with input from all authors. E.D.G., S.M., and S.B. supervised the project. All authors discussed the results and contributed to the final manuscript.

Funding Open access funding provided by Politecnico di Milano within the CRUI-CARE Agreement.

Data Availability No datasets were generated or analysed during the current study.

Declarations

Competing interests The authors declare no competing interests.

References

1. Braghin, F., Bruni, S., Diana, G.: Experimental and numerical investigation on the derailment of a railway wheelset with solid axle. Veh. Syst. Dyn. **44**, 305–325 (2006)
2. Brabie, D.: On the Influence of Rail Vehicle Parameters on the Derailment Process and its Consequences. (2005); Available from: https://urn.kb.se/resolve?urn=urn:nbn:se:kth:diva-242
3. Hung, C., Suda, Y., Aki, M., et al.: Study on detection of the early signs of derailment for railway vehicles. Veh. Syst. Dyn. **48**, 451–466 (2010)

4. Liu, X., Saat, M.R., Barkan, C.P.L.: Analysis of causes of major train derailment and their effect on accident rates. Transp. Res. Rec. **2289**, 154–163 (2012)
5. Wu, X., Chi, M., Gao, H., et al.: Post-derailment dynamic behavior of railway vehicles travelling on a railway bridge during an earthquake. Proc. Inst. Mech. Eng., F J. Rail Rapid Transit **230**, 418–439 (2016)
6. Tanabe, M., Goto, K., Watanabe, T., et al.: An efficient contact model for dynamic interaction analysis of high-speed train and railway structure including derailment during an earthquake. Int. J. Transp. Dev. Integr. **1**, 540–551 (2017)
7. Iwnicki, S., Spiryagin, M., Cole, C., McSweeney, T. (eds.): Handbook of Railway Vehicle Dynamics 2nd edn. CRC Press, Boca Raton (2019)
8. Brabie, D., Andersson, E.: Post-derailment dynamic simulation of rail vehicles – methodology and applications. Veh. Syst. Dyn. **46**, 289–300 (2008)
9. Brabie, D., Andersson, E.: On minimizing derailment risks and consequences for passenger trains at higher speeds. Proc. Inst. Mech. Eng., F J. Rail Rapid Transit **223**, 543–566 (2009)
10. Lai, J., Xu, J., Wang, P., et al.: Numerical investigation on the dynamic behaviour of derailed railway vehicles protected by guard rail. Veh. Syst. Dyn. **59**, 1803–1824 (2021)
11. Bae, H.-U., Yun, K.-M., Lim, N.-H.: Containment capacity and estimation of crashworthiness of derailment containment walls against high-speed trains. Proc. Inst. Mech. Eng., F J. Rail Rapid Transit **232**, 680–696 (2018)
12. Song, I.-H., Kim, J.-W., Koo, J.-S., et al.: Modeling and simulation of collision-causing derailment to design the derailment containment provision using a simplified vehicle model. Appl. Sci. **10**, 118 (2019)
13. Diana, G., Sabbioni, E., Somaschini, C., et al.: Full-scale derailment tests on freight wagons. Veh. Syst. Dyn. **60**, 1849–1866 (2022)
14. Lim, J., Simplified, K.J.: Dynamic FEA simulation for post-derailment train-behaviour estimation through the enhanced input of Wheel–Ballast friction interactions. Appl. Sci. **13**, 6499 (2023)
15. Ling, L., Dhanasekar, M., Thambiratnam, D.P.: Dynamic response of the train–track–bridge system subjected to derailment impacts. Veh. Syst. Dyn. **56**, 638–657 (2018)
16. Ling, L., Dhanasekar, M., Wang, K., et al.: Collision derailments on bridges containing ballastless slab tracks. Eng. Fail. Anal. **105**, 869–882 (2019)
17. Wheel-Sleeper, B.D.: Impact model in rail vehicles analysis. J. Syst. Des. Dyn. **1**, 468–480 (2007)
18. Santelia, M., Mazzeo, F., Di Gialleonardo, E., et al.: A multibody non-linear model of the post-derailment dynamics of a railway vehicle. Veh. Syst. Dyn. **0**, 1–28 (2023)
19. Bekker, M.G.: Theory of Land Locomotion: The Mechanics of Vehicle Mobility. University of Michigan Press, Ann Arbor (2016)
20. Janosi, Z., Hanamoto, B.: The analytical determination of drawbar pull as a function of slip for tracked vehicles in deformable soils (1961)
21. Shampine, L.F., Gordon, M.K.: Computer Solution of Ordinary Differential Equations: The Initial Value Problem. W.H. Freeman, San Francisco (1975)
22. Shampine, L.F., Reichelt, M.W.: The Matlab ODE suite. SIAM J. Sci. Comput. **18**, 1–22 (1997)
23. Shabana, A.A.: Dynamics of Multibody Systems. High. Educ. Camb. Univ. Press. Cambridge University Press, Cambridge (2020)
24. Bruni, S., Vinolas, J., Berg, M., et al.: Modelling of suspension components in a rail vehicle dynamics context. Veh. Syst. Dyn. **49**, 1021–1072 (2011)
25. Przemieniecki, J.S.: Theory of Matrix Structural Analysis. Courier Corporation (1985)
26. Rao, S.S.: Vibration of Continuous Systems. Wiley, New York (2007)
27. Graff, K.F.: Wave Motion in Elastic Solids. Courier Corporation (2012)
28. Lankarani, H., Nikravesh, P.: A contact force model with hysteresis damping for impact analysis of multibody systems. J. Mech. Des. **112**, 369–376 (1990)
29. Jing, G., Siahkouhi, M., Wang, H., et al.: The improvement of the dynamic behavior of railway bridge transition zone using furnace slag reinforcement: a numerical and experimental study. Proc. Inst. Mech. Eng., F J. Rail Rapid Transit **236**, 362–374 (2022)
30. Suhr, B., Marschnig, S., Six, K.: Comparison of two different types of railway ballast in compression and direct shear tests: experimental results and DEM model validation. Granul. Matter **20**, 70 (2018)
31. O'Brien, T.M.J.: Terramechanics: Land Locomotion Mechanics. CRC Press, London (2004)
32. Estaire, J., Santana, M.: Large Direct Shear Tests Performed with Fresh Ballast, pp. 144–161 (2018)